ROYAL SOCIETY
OF CHEMISTRY

Check for updates

β-Cyclodextrin and reduced graphene oxide loaded Ag–TiO₂ composites for enhanced photocatalytic oxidation of urea under sunlight†

Palak Soni,[a] Bonamali Pal[*ab] and Raj Kumar Das [ID] [*ab]

Urea oxidation is important to increase agricultural growth, which can meet food requirements across the world. It is pivotal for converting nitrogen to nitrate that is usable by crops, thus preventing nitrogen loss to the atmosphere. This study focuses on improving the photodegradation efficiency of TiO₂ by incorporating β-CD (beta-cyclodextrin), RGO (reduced graphene oxide), and Ag to enhance nitrate conversion. FT-IR, DRS, PL, EDX, XRD, XPS, HR-TEM DLS, and FESEM were conducted to characterize these materials. Among all the catalysts, the quaternary composite, β-CD/Ag–TiO₂/RGO, exhibited superior performance, achieving an 86.2% degradation efficiency with a 27.8% nitrate yield under sunlight irradiation within 150 min of reaction time. Several factors contribute to the enhanced photoactivity of β-CD/Ag–TiO₂/RGO, including the high surface area and absorptive power of β-CD, the large electronic mobility of RGO, and the localized surface plasmonic resonance effect of Ag, extending the catalyst's response to visible light. An intriguing aspect of this study is the encapsulation of gaseous nitrogen into the hydrophobic interior cavity of β-CD, contributing to the enhancement of urea oxidation. These findings can be very substantial for both agriculturists and chemists, providing valuable insights into designing novel photocatalysts for improved urea oxidation, thereby enhancing agricultural productivity.

1. Introduction

With the projected increase in the global population, there is a growing reliance on fertilizers to meet the escalating demand for crops.[1] Nitrogen-rich fertilizers are fundamental for promoting crop growth, the use of which remains a cornerstone of agricultural practices.[2] Being an easily assimilable form of nitrogen, urea is an extensively used fertilizer that accommodates 46% N content engaged in the mineralization process.[3] Plants primarily uptake nitrogen as nitrate (NO_3^-) and ammonium (NH_4^+) ions. For urea to become assimilable, it undergoes hydrolysis and subsequently forms NH_4^+ ions through protonation, and a further nitrification process begins where nitrite and nitrate form.[4] Plants absorb these ions through specialized transporters that use proton gradients for transportation.[5,6] However, urea exhibits significant losses upon contact with soil compared to other fertilizers, leading to ammonia volatilization, denitrification, runoff, leaching, and other pathways, resulting in the accumulation of reactive nitrogen (organic nitrogen and inorganic nitrogen compounds excluding

N_2).[7,8] Moreover, this unintended ammonia emission diminishes crop yields due to nitrogen loss and poses long-term negative health hazards and environmental consequences as agriculture expands.[9,10] Consequently, the oxidation of urea into beneficial products like NO_3^- is imperative for sustainable agriculture.[11] Hence, there is an urgent need to develop efficient photocatalysts with robust oxidizing capabilities to enhance overall NO_3^- production efficiency. However, urea oxidation to nitrate is an 8-electron transfer process that is very challenging and often affords molecular nitrogen (N_2) as the major product due to partial oxidation. As to increase crop yield, fertilizers are often over-applied, thereby increasing production costs. This can also result in an enhancement of urea concentration in groundwater, resulting in various adverse effects. As a result, different inhibitors have been used to control nitrogen leaching, but their high cost, as well as lack of stability in ambient conditions, limit their practical application.

In this regard, a semiconductor-based photocatalytic process using solar light could be more effective for NO_3^- production yield during urea oxidation to enhance crop yield in agricultural land.[12] Different metal (M)–TiO₂ hybrid nanocatalysts display superior photocatalytic activity, stability and reusability for potential applications in removal of environmental pollutants and production of green energy.[13] Researchers are still attempting to fabricate a better M–TiO₂ nanointerface to improve the photogenerated charge separation efficiency utilizing various synthetic protocols for maximum

[a]Department of Chemistry and Biochemistry, Thapar Institute of Engineering & Technology, Patiala, 147004, Punjab, India. E-mail: bpal@thapar.edu; rkdas@thapar.edu

[b]TIET-Virginia Tech Center of Excellence in Emerging Materials, Thapar Institute of Engineering and Technology, Patiala, 147004, India

† Electronic supplementary information (ESI) available. See DOI: https://doi.org/10.1039/d5na00245a

photocatalytic performance under sunlight. In addition to numerous attempts to reduce the photoexcited electron–hole pair charge recombination process, tuning the M–TiO$_2$ size, shape, surface structural morphology and band energetics is attracting a great deal of current research interest[14] for highly enhanced photocatalytic activity of urea oxidation to NO$_3^-$ (ref. 15) under visible/sunlight irradiation.

The loading of carbon materials like reduced graphene oxide (RGO) over TiO$_2$ could potentially solve these problems.[16] RGO is recognized for its excellent properties, including specific surface area, physicochemical stability, surface flexibility, and low production cost. Moreover, it has high electron mobility and electric capacitance facilitating efficient multi-electron transfer reactions.[17] As a result, it could promote photocatalytic urea oxidation which is an 8-electron transfer process. However, its effectiveness is hindered by agglomeration and restacking due to π–π stacking and van der Waals forces, that reduce its surface area,[18,19] limiting its practical application.

β-Cyclodextrin (β-CD), a well-known supramolecule, is a cyclic oligosaccharide composed of seven glucose units. It is highly adsorbent, non-toxic, and acts as a capping agent to stabilize metals. Urea oxidation frequently results in the formation of N$_2$ as a primary product due to incomplete oxidation. To further improve the efficiency of photocatalysts, it is necessary to design a hybrid system with a strong affinity for N$_2$ and significant oxidizing power, which helps to prevent leaching and improves nitrate production efficiency.[20] β-CD has a toroidal shape with a hydrophilic exterior, exposing –OH groups for hydrogen bonding, and a hydrophobic interior that can encapsulate non-polar guests.[21,22] This distinctive structure of β-CD provides numerous adsorption sites and synergistic interactions, extending its absorption spectrum towards the visible region and reducing the recombination rate.[23] β-CD binds with urea through covalent forces and the hydrophobic interior encapsulates molecular nitrogen very effectively.[24] This mechanistic approach offers stronger interactions, less leaching, and high nitrate yield.

For better charge separation, a photocatalyst should strongly absorb visible light. Adding plasmonic metals such as Ag, Au, or Cu can enhance this ability through localized surface plasmonic resonance (LSPR), which broadens the absorption into the visible spectrum.[25] These transitions enable nanoparticles to absorb sunlight, generating strong electric fields and photogenerated e$^-$/h$^+$ pairs. These pairs can disseminate through phonons, causing a rise in lattice temperatures.[26] High energy charge carriers, electric fields, and elevated temperatures can significantly boost photoactivity.[27] Therefore, the deposition of coinage metals is an effective way to elevate the potential of a prepared material. Interestingly, plasmonic metal-loaded semiconductors are also emerging as new-generation catalysts for nitrogen fixation to yield ammonia.[28–31]

It has been found that literature reports on photocatalytic urea oxidation to yield nitrate are quite limited. Among the reported materials, β-CD/TiO$_2$@Ag NC achieves the highest nitrate yield at 17.8(3)%, while TiO$_2$/RGO yields 9.8(1)% with a NaF additive under neutral pH, which can disrupt ecosystems.[32] This reaction necessitates high electron mobility to maximize the transfer of electrons for enhancing nitrate yield. Consequently, it is vital to develop a new photocatalyst with high capacitance as well as optimum nitrogen binding ability to facilitate urea oxidation. Inspired by these observations, highly proficient ternary (β-CD/Ag–TiO$_2$, Ag–TiO$_2$@RGO, β-CD/TiO$_2$/RGO) and quaternary (β-CD/Ag–TiO$_2$/RGO) heterojunction systems were constructed by using photodeposition and hydrothermal methods. These innovative nanocomposites, with their promising attributes, offer high electron mobility, increased surface area, enhanced optical response, and improved charge separation, thus facilitating a multi-electron transfer pathway of β-CD/Ag–TiO$_2$/RGO for the photooxidation of urea to afford nitrate under visible/sunlight irradiation.

2. Experimental section

2.1 Materials

Graphite powder (98% extra pure); conc. sulfuric acid (H$_2$SO$_4$, 98%); potassium permanganate (KMnO$_4$, 99% extra pure); sodium nitrate (NaNO$_3$, 99%); hydrochloride acid (HCl, 35.4%); L-ascorbic acid (99.5%); hydrogen peroxide (H$_2$O$_2$, 30% (w/v) extra pure); ammonia (NH$_3$, 28%); ethanol (C$_2$H$_5$OH, 99.9%); isopropanol (C$_2$H$_5$O, 99.5%); urea (CO(NH$_2$)$_2$, 99% extra pure) were received from Loba Chemie, India. TiO$_2$ was supplied from Degussa Corporation, Germany. Silver(I) nitrate (AgNO$_3$, ≥99%) was bought from Sigma-Aldrich. β-CD (98.00%) was purchased from GLR innovations. Deionized water (DI) was received from Organo Biotech Laboratories and utilized during all the experimental studies.
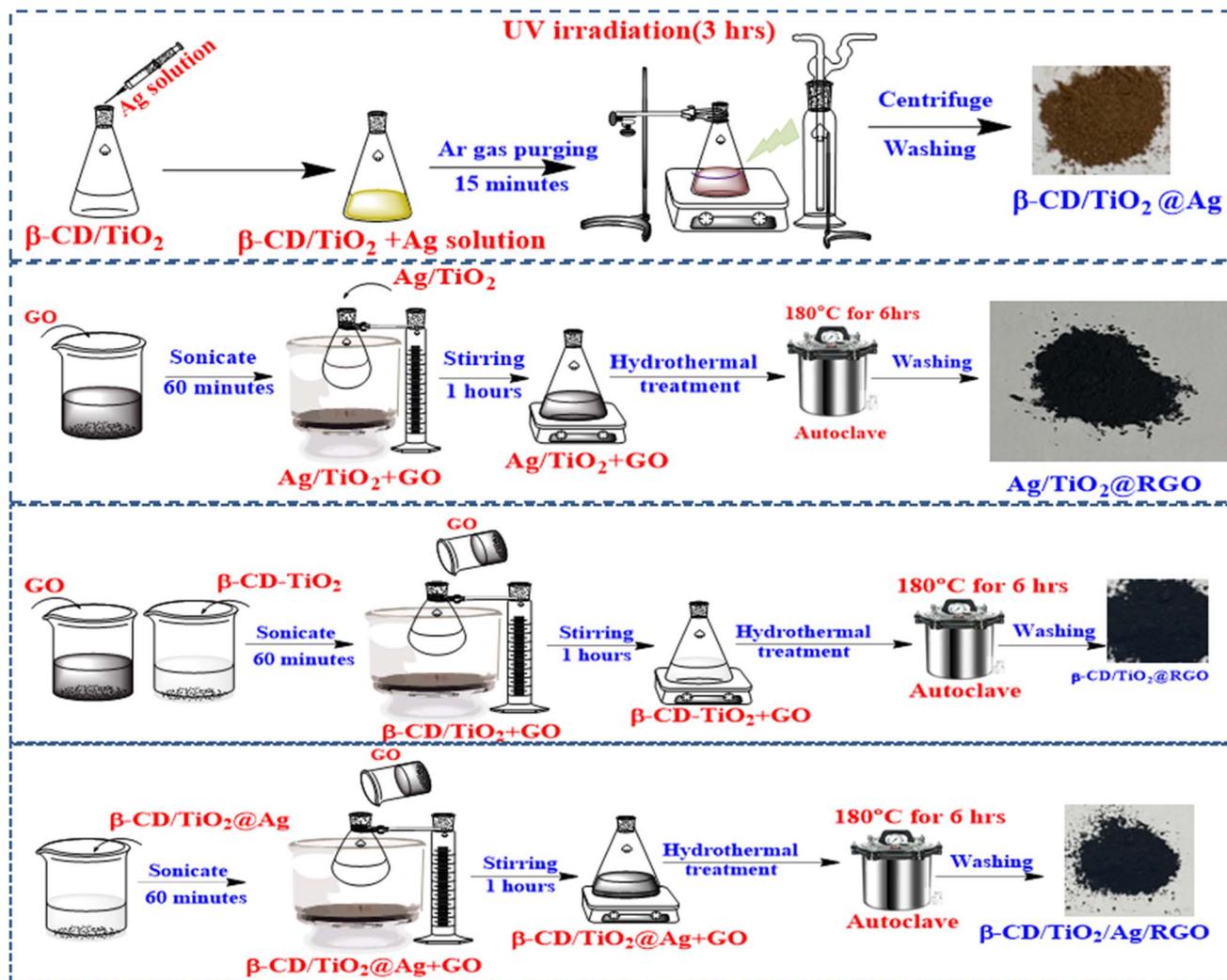
2.2 Synthesis

Preparation of RGO was done by using a reported procedure.[20]

2.2.1 Synthesis of Ag–TiO$_2$. Ag–TiO$_2$ was prepared by a photodeposition method.[33,34] Initially, 934 μL of a solution of AgNO$_3$ in water was added to a suspension of P25 TiO$_2$ in 10 mL of 50% 2-propanol solution in water. Then, Ar was purged in the mixture for 15 min, and the resultant suspension was stirred for 3 h in the presence of radiation from a UV lamp (125 W Hg arc, 10.4 MW cm^{-2}, 300–390 nm). The resultant mixture was centrifuged to afford a solid product which was dried at 55 °C.

2.2.2 Preparation of Ag–TiO$_2$@RGO nanostructures. The preparation of Ag–TiO$_2$@RGO NC was done hydrothermally. About 200 mg of GO powder was dispersed in a small amount of DI water, and then 1 g of Ag/TiO$_2$ was added to it (Scheme 1). After stirring the mixture for 1 h, the uniform suspension was treated hydrothermally at 180 °C for 6 h. The resulting residue was separated by centrifugation followed by drying at room temperature to obtain the Ag/TiO$_2$@RGO nanocomposite, which will be abbreviated as ATR.

2.2.3 Preparation of β-CD/TiO$_2$/RGO nanostructures. An analogous method was applied for synthesizing β-CD/TiO$_2$/RGO NC as described in Section 2.2.2 (Scheme 1). 120 mg of the β-CD/TiO$_2$ composite was added to a 500 mg RGO dispersion under ultrasonication. After stirring the mixture continuously for 1 h, the homogeneous dispersion was treated hydrothermally at 180 °

Scheme 1 A diagram depicting the fabrication of β-CD/Ag–TiO$_2$, Ag–TiO$_2$@RGO, β-CD/TiO$_2$/RGO, and β-CD/Ag–TiO$_2$/RGO nanocomposites.

C for 6 h.[33] The final product was then dried overnight at 30 °C, and this nanocomposite will be referred to as CTR.

2.2.4 Synthesis of β-CD/Ag–TiO$_2$/RGO quaternary nanohybrid. The β-CD/Ag–TiO$_2$/RGO quaternary NC was produced using a hydrothermal method. Initially, 1000 mg of β-CD/Ag–TiO$_2$ was dispersed in a minimal amount of water (Scheme 1). Then, 250 mg of GO was added to the prepared uniform dispersion under ultrasonication. After 1 h of constant stirring, the reaction mixture was subjected to hydrothermal treatment at 180 °C for 6 h.[33] The resultant product was dried overnight at room temperature.[33] This prepared quaternary nanocomposite will be referred to as CTAR.

2.3 Material characterization techniques

The optical absorption of the prepared hybrids was assessed using a Jasco V-750 spectrophotometer with barium sulfate as the reference. Emission properties were analyzed *via* photoluminescence (PL) spectra upon excitation at 340 nm, utilizing a spectrofluorimeter (Shimadzu RF-6000). Structural defects were investigated through Raman spectroscopy using a Horiba

Labram HR confocal micro-Raman spectrophotometer. X-ray diffraction (XRD) patterns were recorded with a Smart Lab SE diffractometer. Field-emission scanning electron microscopy (FESEM) images were recorded with a JEOL JSM-7600F electron microscope. Elemental composition and distribution were analyzed using energy dispersive spectroscopy (EDS, Bruker). High-resolution transmission electron microscopy (HR-TEM) studies were performed with a JEOL JSM-F200. X-ray photoelectron spectroscopy (XPS, PHI 5000 VERSA Probe III) was used to study the chemical environment and oxidation states of the samples. Total organic carbon (TOC) measurements were conducted with a Thermo Scientific HiPer TOC-TN-CLD module to evaluate the demineralization efficiency of CTA, ATR, CTR, and CTAR. Sample aliquots were mixed with H$_3$PO$_4$ (5% w/v) and Na$_2$S$_2$O$_8$ (10% w/v). Then, the reaction mixture was heated in a glass vessel to oxidize all the organic carbon to CO$_2$, which was detected using a non-dispersive infrared (NDIR) detector. The nitrate yield was further estimated using the ultraviolet spectrophotometer screening method (Varian UV0910M156) by monitoring the absorbance at 220 nm.

2.4 Photodegradation analysis

The photocatalytic performance of the ternary and quaternary nanocomposites (NCs) was investigated using urea as the model molecule at an initial concentration of 1.8 mM. Each test was conducted in a series of test tubes, holding 10 mg of catalyst suspended in 10 mL of urea solution. To attain adsorption–desorption equilibrium, the suspensions were stirred vigorously in the dark for 30 min. For urea degradation, the test tubes containing catalysts were kept under sunlight for 150 min in Patiala, India (1–30 May 2023; 12:00 pm–2:30 pm), with average solar radiation of approximately 785 W m^{-2} and temperatures around 35 °C. After 30 min fixed interval, 2 mL of supernatant was collected, and the catalyst was removed by centrifugation at 8000 rpm from the degraded solution. Additionally, urea concentration was estimated using the *p*-dimethylamino-benzaldehyde (DMAB) method.[35]

Urea photodegradation efficiency using the various photocatalysts was calculated using the following equation:

$$\text{Photodegradation efficiency}(\%D) = \frac{C_0 - C_t}{C_0} \times 100 \quad (1)$$

where C_0 and C_t denote the initial and final concemtrations of urea before and after the photocatalytic reaction.[20]

TOC measurements were conducted with a Thermo Scientific HiPer TOC-TN-CLD module to evaluate the demineralization efficiency of CTA, ATR, CTR, and CTAR. The demineralization efficiency (%) was calculated according to the following equation:[36]

$$\text{Demineralization efficiency}(\%) = \frac{\text{TOC}_{\text{initial}} - \text{TOC}_{\text{final}}}{\text{TOC}_{\text{initial}}} \times 100 \quad (2)$$

3. Results and discussion

3.1 Characterizations

3.1.1 Optical absorption. UV-DRS spectra shown in Fig. 1a and S1a† illustrate the optical characteristics of the prepared catalysts. In the DRS patterns of Ag/TiO$_2$ and CTA, a distinct broad band in the visible range (400–500 nm) is observed, accredited to the LSPR effect of Ag nanoparticles.[37,38] The inclusion of RGO in ATR NC not only induces a bathochromic

shift but also improves light absorption in the visible range.[39] Additionally, a strong and broad band is observed for CTR and CTAR NCs due to RGO. In the quaternary composite, the plasmonic band of Ag nanoparticles merges with the RGO band, owing to the extensive absorption range of RGO. This expanded absorption throughout the visible spectrum increases photon availability, generating a higher number of charge carriers and can thereby enhance photocatalytic performance.[40]

The band gap energy of the synthesized ternary and quaternary NCs was determined using Tauc plot (eqn (3)):

$$\alpha h\nu = A(h\nu - E_g)^n \quad (3)$$

where α = absorption coefficient, $h\nu$ = energy of the photon, E_g = band gap, A = energy independent constant, n = Tauc exponent ($n = 1/2$ (indirect band gap)). The E_g values of Ag/TiO$_2$, CTA, ATR, CTR, and CTAR nanocomposites were found to be 2.86, 2.57, 2.38, 2.15, and 1.85 eV, respectively, as shown in Fig. 1b and S1b.† [41] The quaternary NC shows a significantly reduced band gap of 1.85 eV. The reduction in E_g is apparent with the successive addition of RGO, Ag, and β-CD to the TiO$_2$ surface, causing a shift in the optical response towards the visible spectrum. Consequently, this enhancement could improve the photocatalytic performance of the fabricated quaternary NC.

3.1.2 Photoluminescence. To determine the impact of Ag, RGO, and β-CD on charge carrier separation, PL analysis was carried out. Bare TiO$_2$ exhibits two emission bands at 380 nm and 536 nm whereas the Ag/TiO$_2$, CTA, ATR, CTR, and CTAR nanocomposites have smaller emission intensities compared to pristine TiO$_2$ (Fig. 2). The PL results suggest that the lifespan of photoinduced charge carriers in the photocatalysts follows the decreasing order: CTAR > CTR > ATR > CTA > Ag/TiO$_2$ > TiO$_2$. Among all the samples, CTA displayed the highest emission intensity, which suggests a greater rate of recombination and less effective photoinduced charge separation. In contrast, the emission intensity significantly decreases with the addition of Ag, RGO, and β-CD in the nanocomposite. The quenching of PL signals is ascribed to the electron transfer from TiO$_2$ to the surfaces of metallic Ag and RGO. Moreover, RGO's high electrical conductivity facilitates the transfer of electrons, leading to a lower recombination rate.[42,43] Furthermore, β-CD provides
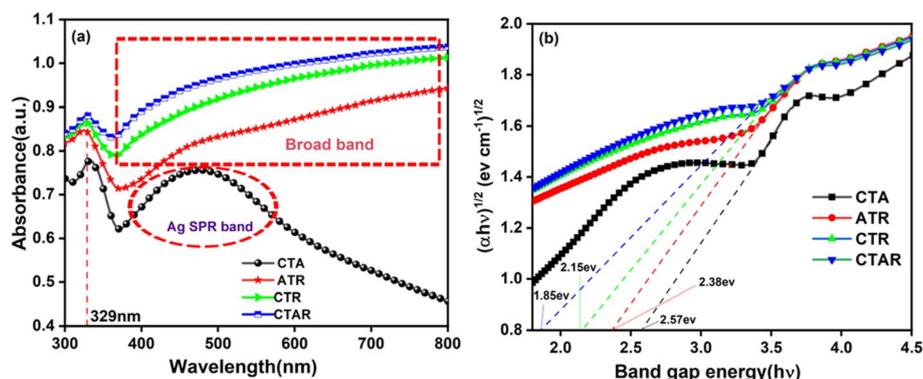

Fig. 1 (a) DRS spectra and (b) Tauc's plots of CTA, ATR, CTR, and CTAR nanocomposites.
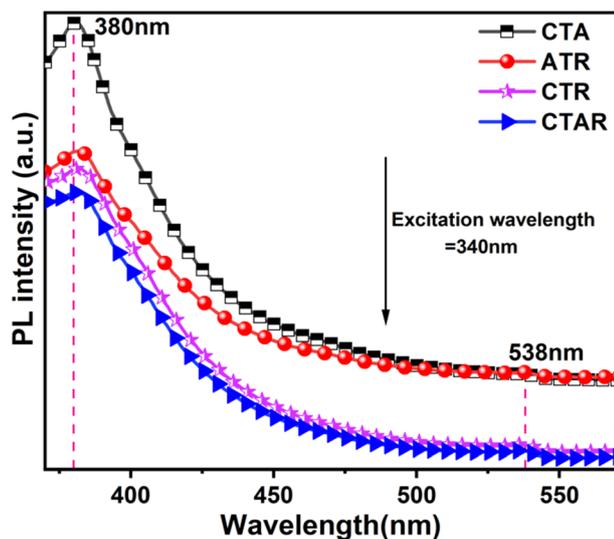
Fig. 2 Photoluminescence spectra of CTA, ATR, CTR, and CTAR nanocomposites.

a favorable environment for prolonging the lifetime of photo-generated charge carriers.[44] The maximum quenching occurred in the quaternary composite, indicating that the synergistic interaction between Ag, RGO, and β-CD creates multiple electron transfer pathways, thus enhancing charge carrier separation and reducing PL peak intensity.

3.1.3 Raman spectral analysis. Fig. 3 illustrates the Raman spectra for CTA, ATR, CTR, and CTAR nanocomposites. The spectra reveal distinct Raman bands for anatase TiO_2 at 145, 390, 518, and 640 cm^{-1}, which are characteristic of the Eg(1), B1g(1), A1g + B1g(2), and Eg(2) optical Raman modes, respectively. In the CTA nanocomposite, β-CD and Ag exhibited no additional active bands. In contrast, the CTR, ATR, and CTAR nanocomposites containing RGO, exhibit D and G bands centered at 1348 and 1598 cm^{-1}. The D band, related to sp^3–C atom vibrations, indicates defects and asymmetry, whereas the
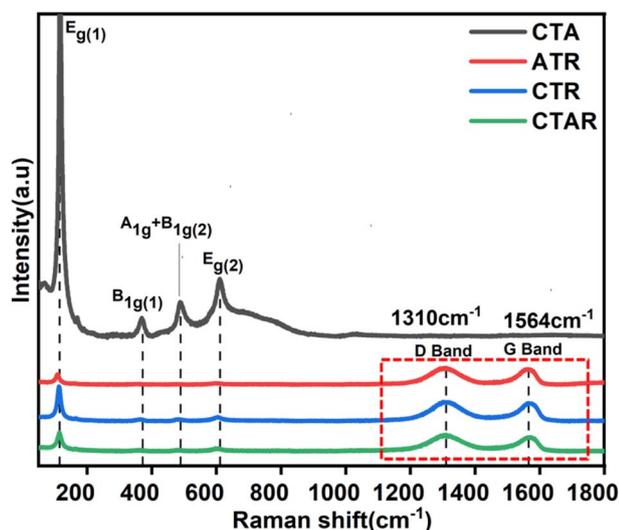
G band, associated with sp^2–C atom vibrations, signifies crystallization and uniformity.[45] The CTAR nanocomposite shows similar Raman bands corresponding to anatase TiO_2 and the G and D bands associated with RGO, confirming the successful formation of the CTAR NC. The peak intensities in the spectra of ATR, CTR, and CTAR are noticeably decreased due to the surface coverage by β-CD and RGO.

3.1.4 XRD patterns. The XRD (Fig. 4) peaks of TiO_2, common across all samples, are located at $2\theta = 25.4$, 37.7, 48, 53.8, 55, 68.7, 70.2, 75.2, and 82.9°, corresponding to the (101), (004), (200), (105), (211), (115), (220), (215), and (301) crystallographic planes of anatase TiO_2 (ICDD card 21-1272). The characteristic peaks observed at $2\theta = 27.4$, 35.8, and 62.8° are assigned to the (110), (103), and (204) planes of the rutile analog (ICDD card no 00-021-1276).[46] The CTR sample exhibited similar diffraction peaks to those of bare TiO_2. Notably, the XRD patterns did not show peaks for β-CD and RGO, likely because C and O have lower X-ray scattering coefficients as compared to silver and titanium. The CTA, ATR, and CTAR nanocomposites displayed signals at $2\theta = 38.2$, 44.3, and 64.1°, correlated to the crystallographic (111), (200), and (220) planes of Ag with face-centered cubic symmetry.[47] The deposition of metallic Ag and β-CD in NCs does not alter any diffraction pattern, indicating the purity and crystallinity of the prepared hybrid photocatalysts.

3.1.5 Structural/morphological studies. The structural and morphological characteristics of the CTA, ATR, CTR, and CTAR NCs were analyzed using the FESEM technique. In Fig. 5a and b, CTA shows a clustered, agglomerated, and spherical structure with Ag nanoparticles embedded on the TiO_2 surface. The presence of a white shell could be attributed to β-CD. The images of ATR display a ruffled and crumpled layered structure. Fig. 5c and d suggests that TiO_2 particles are evenly distributed across the RGO sheets, with spherical Ag nanoparticles (appearing as bright spots) uniformly embedded on the entire RGO surface.[48] In Fig. 5e and f, CTR is seen to have a sheet-like, RGO-based sandwiched structure with TiO_2 particles evenly attached to the RGO layers, and the white lining around the sheet edges may be due to β-CD loading. The FESEM images in Fig. 5g and h show an aggregated, interconnected structure with TiO_2 particles clearly affixed to the RGO surface, and a white lining around the sheets, likely due to β-CD. The Ag nanoparticles are not distinctly visible, which is furthermore corroborated by HRTEM images. The EDX mappings (Fig. S1a–f†) support the occurrence and uniform distribution of all the individual elements in the nanocomposites. The Ag loading on TiO_2 was found to be 0.68 mol% from the EDX spectra (Fig. S1g†).

HRTEM analysis was conducted to investigate the shape, size, and interactions between the components of the quaternary NC. Fig. 6a provides evidence of the layered morphology of RGO sheets. Fig. 6b shows the accumulation of clustered, spherical, and agglomerated metallic Ag deposited on TiO_2 over the RGO layers. The dark spots of metallic Ag, which appear black, range in size from 7 to 21 nm. Fig. 6c and d clearly depicts the white lining of β-CD around the TiO_2 particles and the black spots of metallic Ag firmly attached to the TiO_2 surface.[38] The

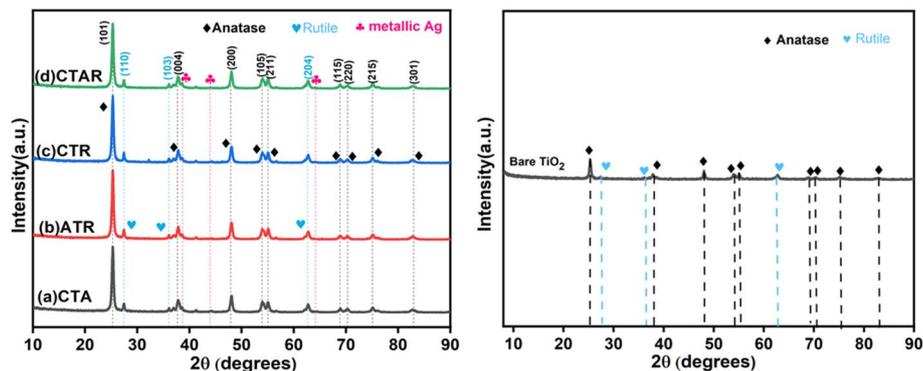**Fig. 3** Raman spectra of CTA, ATR, CTR, and CTAR nanocomposites.

Fig. 4 XRD patterns of (a) CTA, (b) ATR, (c) CTR, and (d) CTAR nanocomposites.
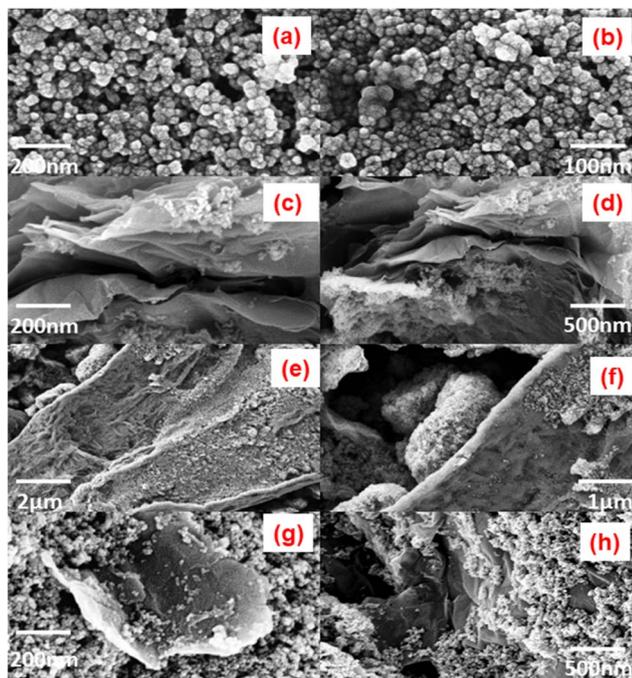

Fig. 5 FESEM images (a)–(h) of CTA, ATR, CTR, and CTAR nanocomposites at different magnifications.

RGO sheets serve as a substrate for the integrated photo-deposited Ag on the TiO_2 nanoparticles.[49] Fig. 6e shows two sets of lattice fringes: 0.36 nm for the (101) plane of TiO_2 and 0.23 nm for the (111) plane of Ag(0). Fig. 6f presents the SAED pattern, displaying concentric rings with bright spots analogous with the TiO_2 (110), (101), and metallic Ag (111), (200) diffraction planes of the CTAR nanocomposite.

3.1.6 XPS analysis. XPS analysis (Fig. 7) confirms the presence of C, O, Ti, and Ag in the CTAR hybrid composite. The C 1s spectrum (Fig. 7) contains characteristic peaks at 284.7, 286.0, and 288.6 eV for the aliphatic, ethereal, and carbonyl carbons respectively. The O 1s spectrum (Fig. 7c) shows peaks at 529.8 and 532.1 eV, corresponding to titanium- and carbon-bound oxygen atoms, respectively. The Ti 2p signals (Fig. 7d) at 458.6 eV and 464.3 eV suggest the presence of tetravalent

titanium with a difference in binding energy of 5.7 eV. Notably, the Ti 2p spectrum also includes one additional signal at 460.0 eV corresponding to Ti–C bonding. The Ag 3d spectrum shows peaks at 367.9 eV and 373.9 eV, with a splitting of 6.0 eV, confirming the occurrence of zerovalent silver in the CTAR nanocomposite. Moreover, the loading of silver on TiO_2 was observed to be 0.68%, which is consistent with the results obtained from EDX spectra.

3.1.7 FT-IR studies. To identify the different functional groups, FT-IR studies were performed (Fig. S3a and b†). The O–H stretching vibrational modes of β-CD-loaded ternary and quaternary heterostructures (3343 cm^{-1}) are shifted towards higher energy compared to bare β-CD. Such observation reveals that the binding of TiO_2 increases the structural rigidity of β-CD thereby increasing the vibrational frequencies. For β-CD/TiO_2@Ag, strong –OH stretching at 3343 cm^{-1} and Ti–O–C bands below 1000 cm^{-1} indicate the interaction between β-CD and TiO_2 with Ag nanoparticles. Ag/TiO_2@RGO shows
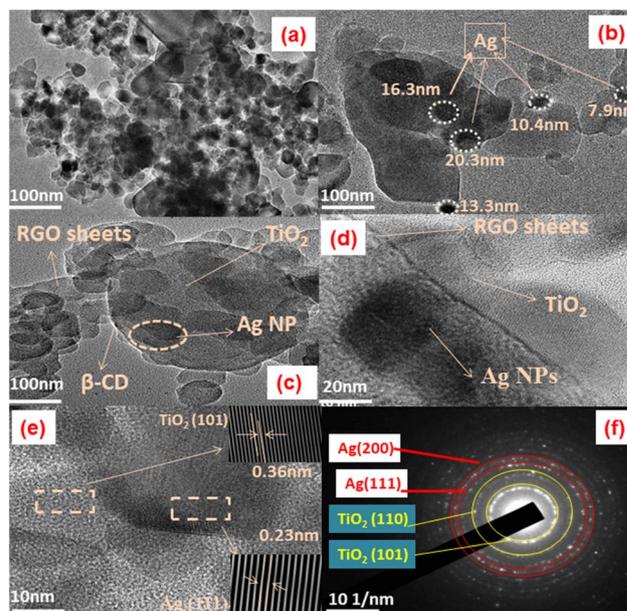

Fig. 6 HRTEM images showing structural morphology (a)–(d), lattice fringes (e), and SAED pattern (f) of the CTAR nanocomposite.
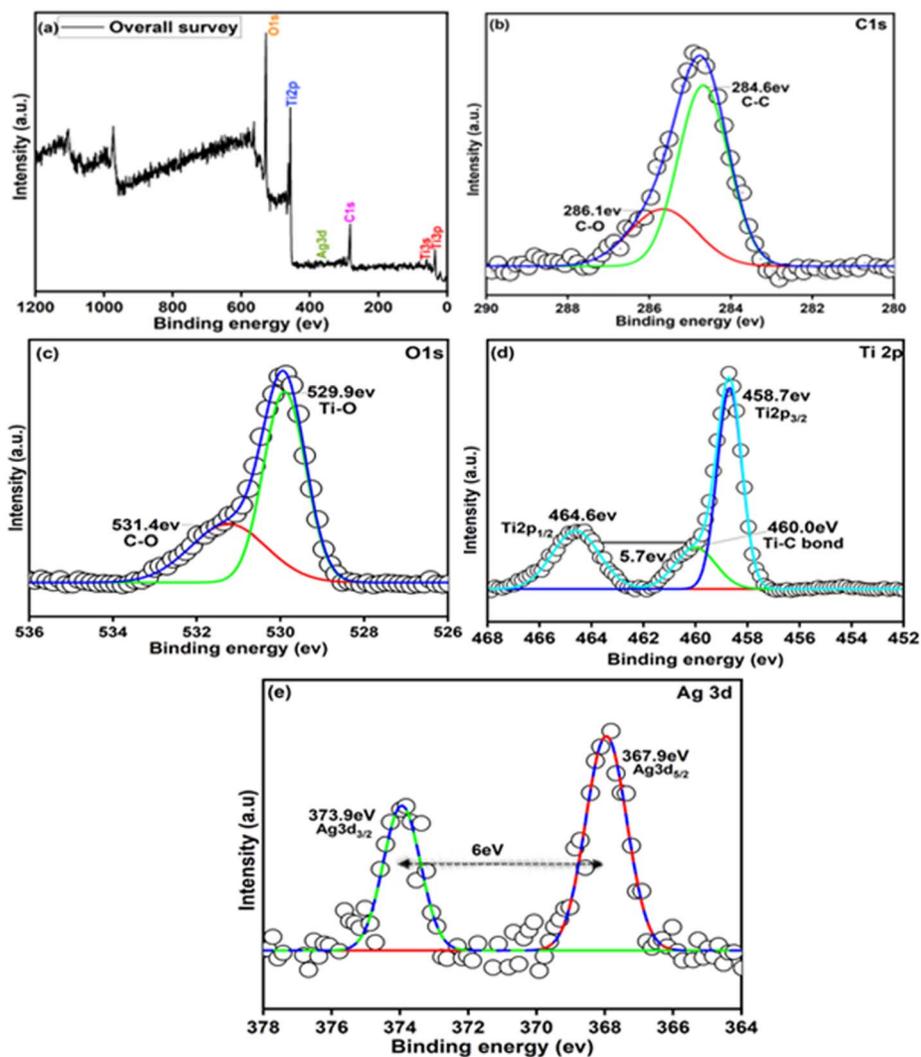
Fig. 7 XPS spectra showing (a) overall survey spectrum; (b) C 1s; (c) O 1s; (d) Ti 2p; (e) Ag 3d of the CTAR quaternary heterostructure.

characteristic peaks at 1716 cm^{-1} (C=O) and 1582 cm^{-1} (C=C), confirming the presence of RGO, along with Ti–O–C bonds suggesting TiO$_2$-RGO interactions. β-CD/TiO$_2$@RGO exhibits –OH stretching band at 3343 cm^{-1} and C=O/C=C peaks, reflecting contributions from β-CD and RGO, coupled with strong Ti–O–C signals. In the spectrum of β-CD/TiO$_2$/Ag/RGO, the presence of –OH, C–H, and Ti–O–C peaks highlights enhanced interactions between β-CD, TiO$_2$, RGO, and Ag nanoparticles, demonstrating the composite's robust structural integration.

3.2 Photooxidation of urea

The efficiencies of the CTA, ATR, CTR, and CTAR NCs were assessed in photocatalytic urea oxidation. Fig. 8 shows the adsorption and photodegradation curves for the various nanocomposites after 150 min of reaction time. The adsorption capacity of the catalysts showed a progressive increase in the following sequence: CTA < ATR < CTR < CTAR. This improvement is likely due to the incorporation of new guest binding sites arising from the deposition of β-CD, RGO, and Ag

nanoparticles (Fig. S4† and 8a). Once equilibrium was achieved, the catalytic activity was examined under sunlight (Fig. S5† and 8b). Sunlight exposure enhanced the photoactivity of all the catalysts, where the quaternary composite (CTAR) exhibited the highest degradation after 150 min of sunlight exposure.

The oxidation of urea involves the transfer of 8 electrons to form nitrate.[20] The composites incorporate RGO, which has high electron mobility, facilitating electron transfer and enhancing photoinduced charge separation. β-CD provides a substantial number of sites for urea binding, which results in reduced nitrogen leaching. Moreover, the deposition of Ag nanoparticles enhances light absorption due to the LSPR effect.[32,50]

The modification with different components in all the catalysts altered the oxidation trend, as shown in Fig. 8c, following the order: CTAR (86.2%) > CTR (75.8%) > ATR (70.5%) > CTA (55.7%). The observed data were analyzed according to a pseudo-first-order kinetic equation:[51]
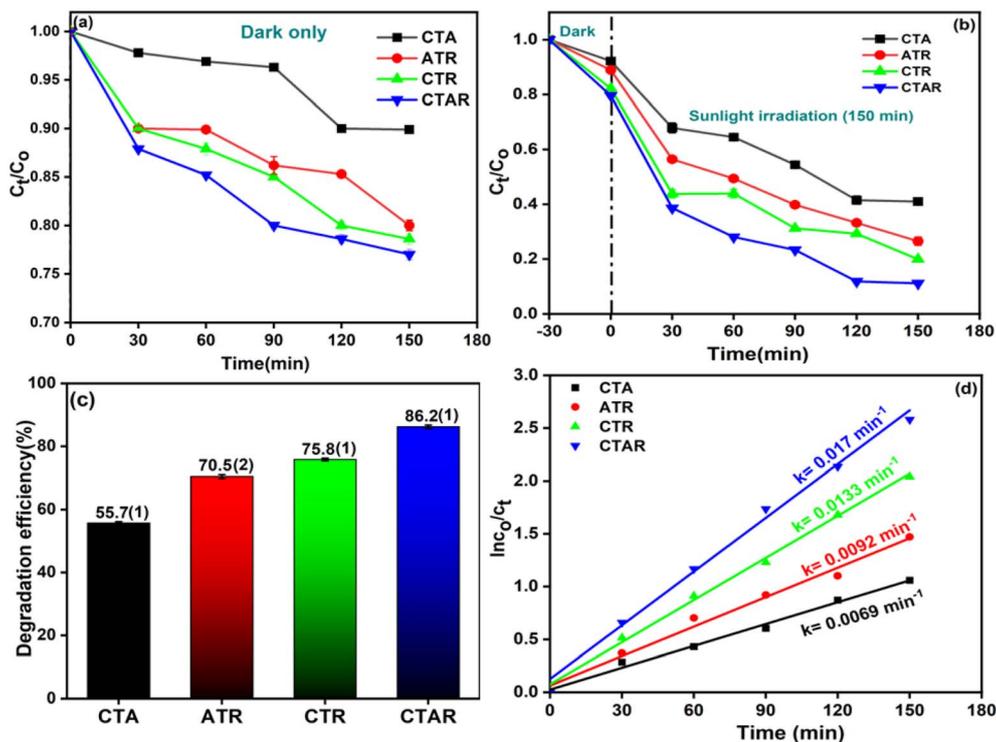
$$\ln \frac{C_0}{C_t} = kt \tag{4}$$

Fig. 8 Variation of urea concentration (a) in the dark and (b) under sunlight irradiation. (c) Comparison of degradation efficiency and (d) pseudo-first-order kinetic fitting for CTA, ATR, CTR, and CTAR nanocomposites.

where C_0 = initial concentration, C_t = concentration at time t, k = pseudo-first-order rate constant (min^{-1}).

The rate constant (min^{-1}) for urea oxidation followed the order: CTA (0.0069) < ATR (0.0092) < CTR (0.0133) < CTAR (0.017). Among all the nanocomposites, CTAR exhibits the highest rate of photocatalytic reaction. The combined components in the CTAR nanocomposite contributed to the improved photocatalytic activity.

3.3 Demineralization efficiency and nitrate yields

It is clear that the oxidation of urea does not necessarily lead to complete mineralization into CO_2 and H_2O. Therefore, it is crucial to assess the demineralization efficiency[52,53] (eqn (2)). Fig. 9a presents the results of urea oxidation using bare CTA (54%), ATR (69.7%), CTR (75%), and CTAR (85%) over 150 min under sunlight irradiation. The CTAR nanocomposite demonstrates the highest demineralization efficiency (85%) of urea which aligns closely with the degradation efficiency suggesting its complete photodegradation.

The principal aim of this study is to improve the overall yield of NO_3^- using potential photocatalysts. The oxidation of urea was conducted using CTA, ATR, CTR, and CTAR under sunlight for 150 min to determine the NO_3^- yield. The results depicted in Fig. 9b illustrate the NO_3^- yield achieved by these photocatalysts. Remarkably, the CTAR nanocomposite exhibits the highest NO_3^- yield at 27.8%. The synergistic effect of silver, RGO, and β-CD loading demonstrates greater solar light absorption, increases electron–hole pair lifetime, and minimizes nitrogen leaching.[54]
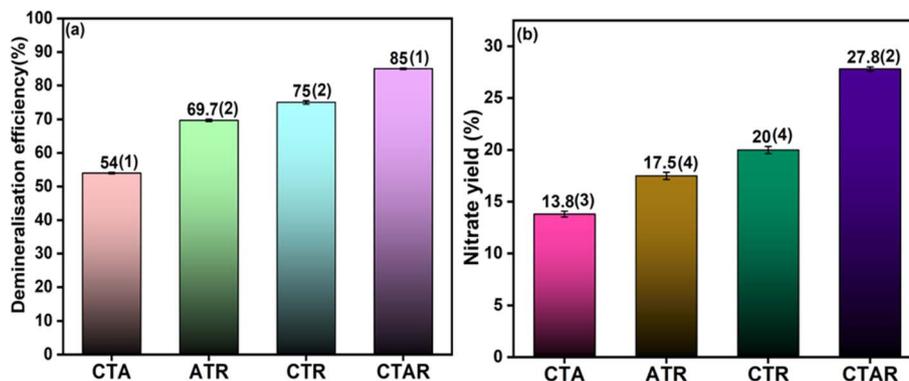

Fig. 9 Comparison of (a) demineralization efficiency and (b) nitrate yield for the different hybrid composites.

Table 1 Comparison of urea degradation and nitrate yield for the CTAR quaternary nanocomposite with reported photocatalysts

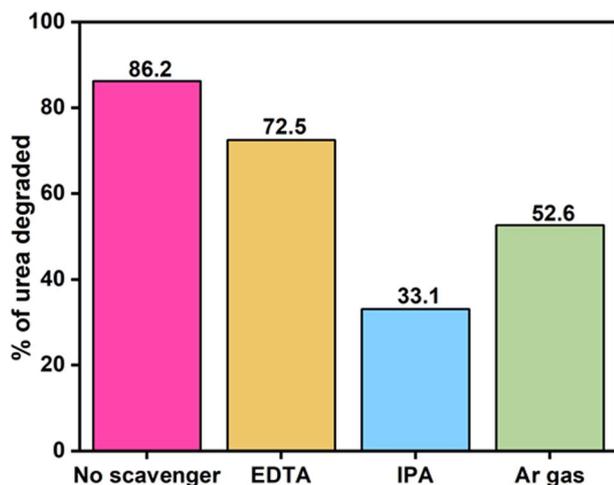| Photocatalyst	Urea degradation efficiency (%)	Nitrate yield (%)	Reference
N-Doped TiO$_2$/polystyrene	70	0.37	55
RGO/TiO$_2$	66(1)	9.8(1)	20
β-CD$_{25}$/TiO$_2$@Ag$_1$	78(1)	17.8(3)	32
CTAR	85(1)	27.8(2)	This work

Fig. 10 Effect of scavenger addition in the photocatalytic urea degradation efficiencies of the CTAR quaternary heterostructure.

It found that the CTAR quaternary hybrid exhibits the highest urea degradation efficiency and nitrate yield (%) compared to previously reported photocatalysts (Table 1).

3.4 Scavenger studies

Various scavengers, such as EDTA, IPA, and argon gas, were selected to reveal the roles of various reactive species.[56] Scavenging experiments were conducted during the urea oxidation over the CTAR photocatalyst under similar conditions (Fig. 10). As depicted in Fig. 10, the degradation rate significantly decreased in the presence of IPA and argon gas, indicating that $^{\bullet}$OH and O$_2^-$ act as the essential active species in the oxidation of urea. Conversely, the rate of degradation also decreased with the EDTA scavenger, although the reduction was lesser, suggesting that the holes (h$^+$) have minor participation in the oxidation process.

3.5 Mechanistic details

The band gap energy (E_g) values obtained from the DRS analysis were utilized to calculate the valence band (VB) and conduction band (CB) positions at the point of zero charge using the following equations (Scheme 2):

$$E_{VB} = \chi - E^e + 0.5\,E_g \qquad (5)$$

$$E_{CB} = E_{VB} - E_g \qquad (6)$$

where E_{CB} = conduction band edge, E_{VB} = valence band edge, E_g = energy of the bandgap, E^e = free electron energy (4.5 eV $vs.$ NHE), χ = absolute electronegativity of photocatalyst (5.81 $vs.$ NHE for TiO$_2$).

The photodegradation mechanism of the β-CD-containing CTAR composite for urea degradation can be explained based on the band positions of TiO$_2$. The CB is positioned at −0.385 eV and the VB is at +2.235 eV, relative to the NHE. Upon sunlight irradiation, TiO$_2$ does not absorb significantly due to a large band gap. However, the incorporation of Ag substantially
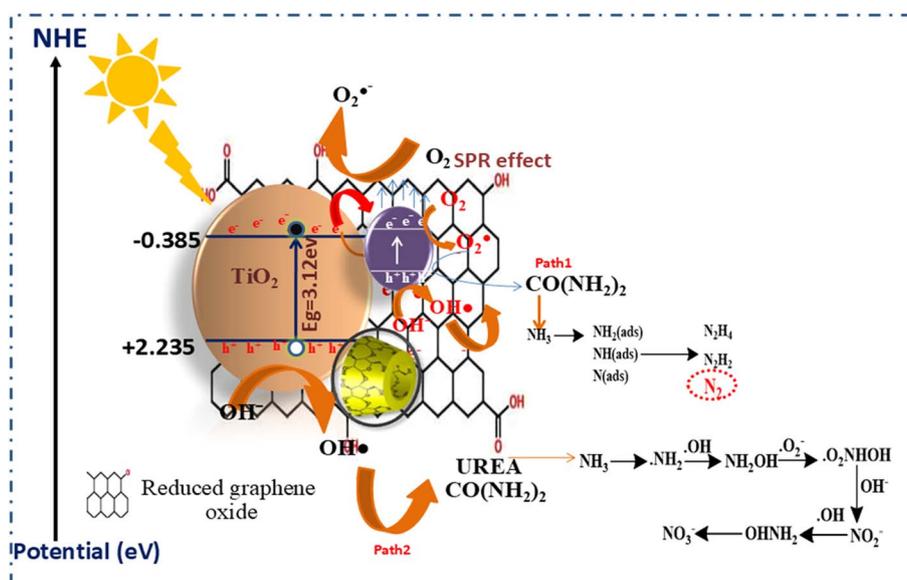
Scheme 2 Schematic representation showing the relative band positions and the photocatalytic activity of the CTAR composite.

enhanced the visible light sensitization of TiO$_2$ due to the SPR phenomenon. The interaction of sunlight with Ag induced a collective oscillation of its conduction electrons, generating a localized electric field. This effect facilitated the efficient separation of photogenerated electron–hole (e$^-$/h$^+$) pairs on the TiO$_2$ surface, thereby transforming it into a visible-light-active photocatalyst. In the presence of Ag nanoparticles and RGO, these electrons are efficiently separated and transported, reducing recombination rates. Ag acts as an electron sink, while RGO facilitates charge transfer due to its excellent conductivity. As the CB edge potential is much more negative than that of O$_2$/O$_2$$^{\cdot-}$ (−0.046 eV), there is a facile reduction of dissolved oxygen to form superoxide anions. Similarly, the VB edge potential is more positive than that of $^{\cdot}$OH/H$_2$O (+2.68 eV), allowing the oxidation water to produce hydroxyl ($^{\cdot}$OH) radicals. These reactive oxygen species (ROS) effectively break down urea into NO$_3$$^-$ and less harmful byproducts. Additionally, β-CD enhances the photocatalytic efficiency by forming inclusion complexes with urea molecules, increasing their local concentration near the photocatalyst's active sites and improving the degradation efficiency. This synergistic effect makes the composite highly effective for the photodegradation of urea.

The mechanism involves the synergistic interaction between Ag, Ti, and RGO as shown in Scheme 3. Photoexcited electrons from the TiO$_2$ CB swiftly migrate to Ag and RGO, preventing photoelectron pair recombination and increasing charge carriers to form reactive species (O$_2$$^-$, $^{\cdot}$OH), thus boosting photocatalytic performance. The two-dimensional RGO structure provides excellent conductivity, facilitating rapid charge

transport and separation. Ag nanoparticles generate high-energy electrons with the LSPR effect, which undergo fast transfer to the RGO surface. These electrons react with adsorbed oxygen to form superoxide ions (O$_2$$^-$), while excited holes oxidize with H$_2$O to produce hydroxyl radicals ($^{\cdot}$OH). Both species are important for urea degradation.[48]

Urea molecules first interact noncovalently with the hydroxyl groups of β-CD (step 1) and are oxidized to produce molecular nitrogen (N$_2$) (step 2). This nitrogen binds to the hydrophobic region of β-CD (step 3), which helps minimize nitrogen leaching. Following this, the nitrogen bound to β-CD undergoes further oxidation, resulting in the formation of nitrate (step 4). The final step (step 5) is associated with the release of nitrate to regenerate the original photocatalyst.

3.6 Reusability and stability studies

The practical applicability of a catalyst is often assessed based on its recyclability and stability. Herein, the recyclability of the CTAR catalyst was evaluated over four cycles under sunlight. As shown in Fig. 11a, the CTAR NC's degradation efficiency dropped by only 9% after four cycles, highlighting its potential as a reusable catalyst. The slight decline in photocatalytic performance could be attributed to the loss of photocatalyst mass during successive experiments.

Furthermore, the structural stability of the catalyst was also evaluated to support this assertion. Fig. 11b displays the XRD patterns of the CTAR nanocomposite before and after photocatalytic degradation reactions. No shifts in peak positions or
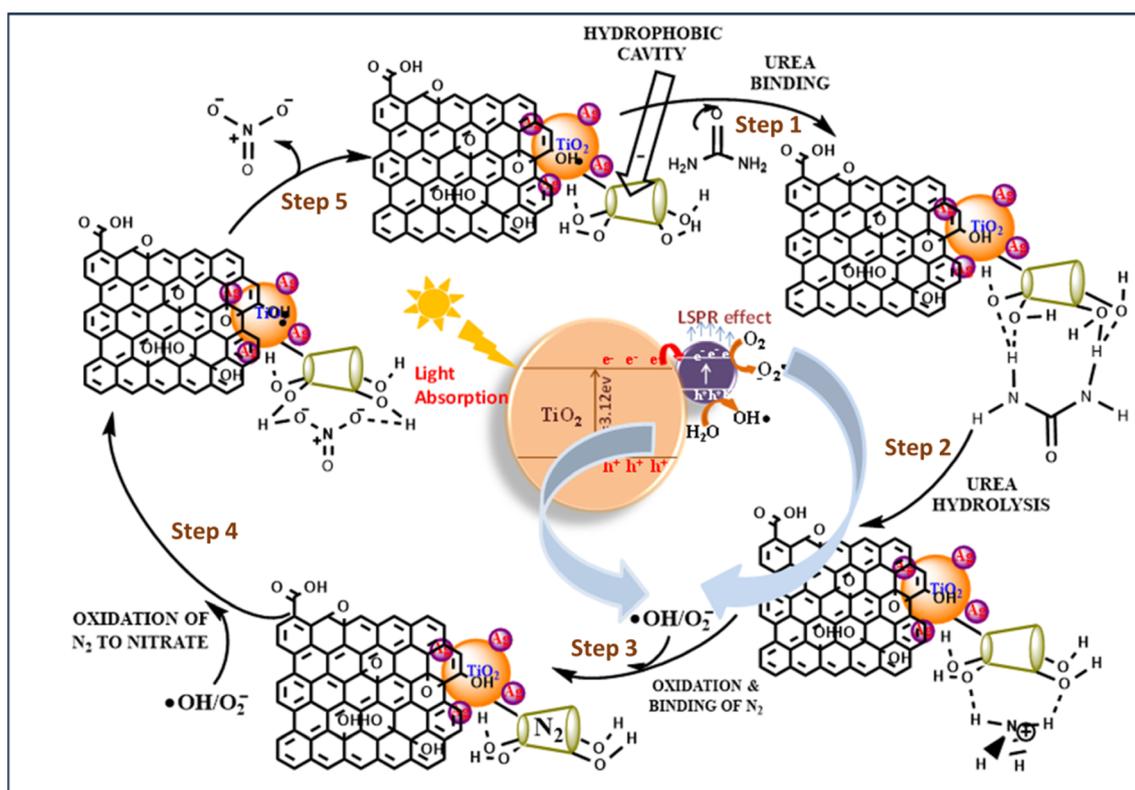
Scheme 3 Detailed mechanism for urea oxidation catalyzed by the β-CD/TiO$_2$/Ag/RGO (CTAR) quaternary composite.
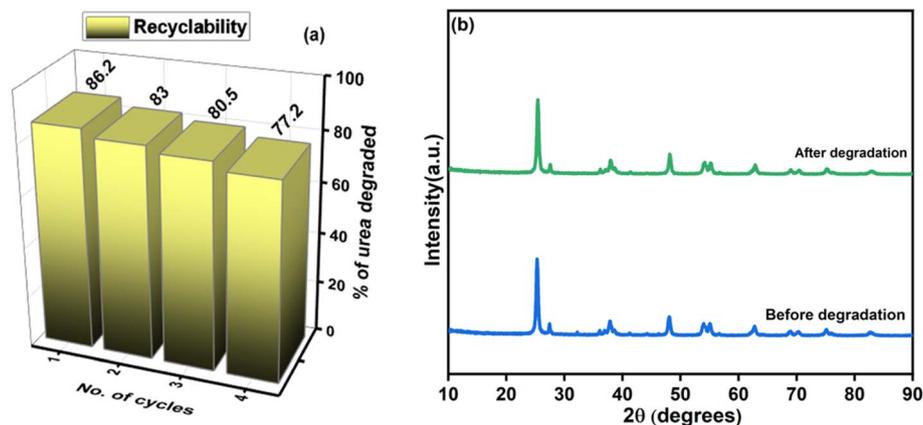
Fig. 11 (a) Recyclability of the CTAR NC for urea degradation under sunlight over four consecutive cycles. (b) XRD patterns showing the stability of the CTAR NC before and after degradation.

changes in peak intensities were observed, indicative of structural integrity. Therefore, the CTAR NC is considered an excellent material for the photocatalytic oxidation of urea.

4. Conclusion

Novel ternary and quaternary nanocomposites incorporating Ag, RGO, and β-CD were synthesized for the first time and extensively studied with the aim of enhancing the photocatalytic oxidation of urea. Among these, the CTAR quaternary nanocomposite demonstrated exceptional photocatalytic efficiency, achieving 86.2% degradation within 150 min under solar light, surpassing that of the other ternary nanocomposites. The incorporation of Ag extended the visible light sensitivity of TiO_2, β-CD facilitated nitrogen binding through hydrophobic interactions to minimize nitrogen leaching, and RGO provided high capacitance and electron mobility while preventing rapid recombination of photogenerated charge carriers. The synergistic interactions among TiO_2, Ag, β-CD, and RGO contributed to the superior photocatalytic performance of the quaternary nanocomposite. Furthermore, the catalyst exhibited remarkable stability and recyclability. This study underscores the potential of the CTAR composite as a green, solar light-activated catalyst for enhancing the photocatalytic oxidation of urea.

Data availability

The supporting data have been uploaded as a part of the ESI.†

Author contributions

Palak soni: conceptualization, performance, methodology, experiments, execution, data collection, data correction, writing the original draft. Bonamali Pal: supervision, data investigation, data validation, reviewing, and editing. Raj Kumar Das: supervision, data investigation, data validation, reviewing, and editing.

Conflicts of interest

The authors declare that they have no known competing financial interests or personal relationships that could have appeared to influence the work reported in this paper.

Acknowledgements

References

1 J. Penuelas, F. Coello and J. Sardans, A better use of fertilizers is needed for global food security and environmental sustainability, *Agric. Food Secur.*, 2023, **12**, 1–9.

2 S. J. Leghari, N. A. Wahocho, G. M. Laghari, A. H. Laghari, G. M. Bhabhan, K. H. Talpur and A. A. Lashari, Role of nitrogen for plant growth and development: a review, *Adv. Environ. Biol.*, 2016, **10**, 209–218.

3 P. Shetty, C. Acharya and N. Veeresh, Effect of urea fertilizer on the biochemical characteristics of soil, *Int. J. Appl. Sci. Biotechnol.*, 2019, **7**, 414–420.

4 C. Masclaux-Daubresse, F. Daniel-Vedele, J. Dechorgnat, F. Chardon, L. Gaufichon and A. Suzuki, Nitrogen uptake, assimilation and remobilization in plants: challenges for sustainable and productive agriculture, *Ann. Bot.*, 2010, **105**, 1141–1157.

5 Y. S. Ku, S. S. Cheng, M. S. Ng, G. Chung and H. M. Lam, The tiny companion matters: the important role of protons in active transports in plants, *Int. J. Mol. Sci.*, 2022, **23**, 2824.

6 T. Ketehouli, K. F. I. Carther, M. Noman, F. W. Wang, X. W. Li and H. Y. Li, Adaptation of plants to salt stress: characterization of Na+ and K+ transporters and role of Cbl

gene family in regulating salt stress response, *Agronomy*, 2019, **9**, 687.

7 M. Skorupka and A. Nosalewicz, Ammonia volatilization from fertilizer urea—A new challenge for agriculture and industry in view of growing global demand for food and energy crops, *Agriculture*, 2021, **11**, 822.

8 Z. Ma, Y. Yue, M. Feng, Y. Li, X. Ma, X. Zhao and S. Wang, Mitigation of ammonia volatilization and nitrate leaching *via* loss control urea triggered H-bond forces, *Sci. Rep.*, 2019, **9**, 1–9.

9 Y. Liu, Y. Ge, J. Tan, H. Wang and Y. Ding, Research on ammonia emissions characteristics from light-duty gasoline vehicles, *J. Environ. Sci.*, 2021, **106**, 182–193.

10 M. Anas, F. Liao, K. K. Verma, M. A. Sarwar, A. Mahmood, Z. L. Chen, Q. Li, X. P. Zeng, Y. Liu and Y. R. Li, Fate of nitrogen in agriculture and environment: agronomic, eco-physiological and molecular approaches to improve nitrogen use efficiency, *Biol. Res.*, 2020, **53**, 1–20.

11 Y. Jiang, Y. Zhu, W. Lin and J. Luo, Urea fertilization significantly promotes nitrous oxide emissions from agricultural soils and is attributed to the short-term suppression of nitrite-oxidizing bacteria during urea hydrolysis, *Microorganisms*, 2024, **12**, 685.

12 F. Zhang, X. Wang, H. Liu, C. Liu, Y. Wan, Y. Long and Z. Cai, Recent advances and applications of semiconductor photocatalytic technology, *Appl. Sci.*, 2019, **9**, 2489.

13 S. A. Mousa, H. Abdallah and S. A. Khairy, Low-cost photocatalytic membrane modified with green heterojunction TiO_2/ZnO nanoparticles prepared from waste, *Sci. Rep.*, 2023, **13**, 1–19.

14 L. Lu, G. Wang, Z. Xiong, Z. Hu, Y. Liao, J. Wang and J. Li, Enhanced photocatalytic activity under visible light by the synergistic effects of plasmonics and Ti^{3+}-doping at the Ag/TiO_{2-x} heterojunction, *Ceram. Int.*, 2020, **46**, 10667–10677.

15 G. Shao, Y. Zang and B. J. Hinds, TiO_2 nanowires based system for urea photodecomposition and dialysate regeneration, *ACS Appl. Nano Mater.*, 2019, **2**, 6116–6123.

16 H. Liu, P. Li, H. Bai, C. Du, D. Wei, Y. Su, Y. Wang and L. Yang, Incorporation of reduced graphene oxide into faceted flower-like (001) TiO_2 for enhanced photocatalytic activity, *R. Soc. Open Sci.*, 2015, **5**, 180613.

17 W. Liu and G. Speranza, Tuning the oxygen content of reduced graphene oxide and effects on its properties, *ACS Omega*, 2021, **6**, 6195–6205.

18 R. Geetha Bai, K. Muthoosamy, F. N. Shipton and S. Manickam, Acoustic cavitation induced generation of stabilizer-free, extremely stable reduced graphene oxide nanodispersion for efficient delivery of paclitaxel in cancer cells, *Ultrason. Sonochem.*, 2017, **36**, 129–138.

19 K. I. Nargatti, S. S. Ahankari, J. R. C. Dizon and R. T. Subramaniam, Environmentally friendly water-based reduced graphene oxide/cellulose nanofiber ink for supercapacitor electrode applications, *ACS Omega*, 2024, **9**, 11730–11737.

20 P. Soni, B. Pal and R. K. Das, Enhanced photocatalytic urea oxidation under neutral medium by reduced graphene oxide coated TiO_2 nanoparticles, *Catal. Commun.*, 2023, **179**, 106690.

21 M. Chen, Y. Meng, W. Zhang, J. Zhou, J. Xie and G. Diao, β-Cyclodextrin polymer functionalized reduced-graphene oxide: application for electrochemical determination imidacloprid, *Electrochim. Acta*, 2013, **108**, 1–9.

22 X. Tu, F. Gao, X. Ma, J. Zou, Y. Yu, M. Li, F. Qu, X. Huang and L. Lu, Mxene/carbon nanohorn/β-cyclodextrin-Metal-organic frameworks as high-performance electrochemical sensing platform for sensitive detection of carbendazim pesticide, *J. Hazard. Mater.*, 2020, **396**, 122776.

23 P. Sakthivel and P. Velusamy, Modification of the photocatalytic performance of various metal oxides by the addition of β-cyclodextrin under visible light irradiation, *J. Water Process Eng.*, 2017, **16**, 329–337.

24 A. Szwajca and H. Koroniak, Encapsulation of fluoroaromatics by β-cyclodextrin and their derivatives theoretical studies, *J. Fluorine Chem.*, 2014, **167**, 122–127.

25 I. Ibrahim Zamkoye, B. Lucas and S. Vedraine, Synergistic effects of localized surface plasmon resonance, surface plasmon polariton, and waveguide plasmonic resonance on the same material: a promising hypothesis to enhance organic solar cell efficiency, *Nanomaterials*, 2023, **13**, 2209.

26 I. Ahmed, L. Shi, H. Pasanen, P. Vivo, P. Maity, M. Hatamvand and Y. Zhan, There is plenty of room at the top: generation of hot charge carriers and their applications in perovskite and other semiconductor-based optoelectronic devices, *Light Sci. Appl.*, 2021, **10**, 1–28.

27 Y. Hattori, J. Meng, K. Zheng, A. Meier De Andrade, J. Kullgren, P. Broqvist, P. Nordlander and J. Sá, Phonon-assisted hot carrier generation in plasmonic semiconductor systems, *Nano Lett.*, 2021, **21**, 1083–1089.

28 P. Xing, S. Wu, Y. Chen, P. Chen, X. Hu, H. Lin, L. Zhao and Y. He, New application and excellent performance of Ag/$KNbO_3$ nanocomposite in photocatalytic NH3 synthesis, *ACS Sustainable Chem. Eng.*, 2019, **7**, 12408–12418.

29 X. Li, L. Chen, J. Wang, J. Zhang, C. Zhao, H. Lin, Y. Wu and Y. He, Novel platinum-bismuth alloy loaded $KTa_{0.5}Nb_{0.5}O_3$ composite photocatalyst for effective nitrogen-to-ammonium conversion, *J. Colloid Interface Sci.*, 2022, **618**, 362–374.

30 J. Zhang, L. Yue, Z. Zeng, C. Zhao, L. Fang, X. Hu, H. Lin, L. Zhao and Y. He, Preparation of $NaNbO_3$ microcube with abundant oxygen vacancies and its high photocatalytic N_2 fixation activity in the help of Pt nanoparticles, *J. Colloid Interface Sci.*, 2023, **636**, 480–491.

31 L. Chen, W. Zhang, J. Wang, X. Li, Y. Li, X. Hu, L. Zhao, Y. Wu and Y. He, High piezo/photocatalytic efficiency of Ag/Bi_5O_7I nanocomposite using mechanical and solar energy for N_2 fixation and methyl orange degradation, *Green Energy Environ.*, 2023, **8**, 283–295.

32 P. Soni, B. Pal and R. K. Das, Influence of β-CD and Ag deposition over TiO_2 towards photocatalytic oxidation of urea under solar irradiation, *J. Environ. Chem. Eng.*, 2024, **12**, 112150.

33 K. H. Leong, L. C. Sim, D. Bahnemann, M. Jang, S. Ibrahim and P. Saravanan, Reduced graphene oxide and Ag wrapped

TiO$_2$ photocatalyst for enhanced visible light photocatalysis, *APL Mater.*, 2015, **3**, 104503.

34 S. Bhardwaj, D. Sharma, P. Kumari and B. Pal, Influence of photodeposition time and loading amount of Ag co-catalyst on growth, distribution and photocatalytic properties of Ag@TiO$_2$ nanocatalysts, *Opt. Mater.*, 2020, **106**, 109975.

35 J. D. Giraldo and B. L. Rivas, Determination of urea using p-*N*,*N*-dimethylaminobenzaldehyde: solvent effect and interference of chitosan, *J. Chil. Chem. Soc.*, 2017, **62**, 3538–3542.

36 L. Rimoldi, D. Meroni, E. Falletta, V. Pifferi, L. Falciola, G. Cappelletti and S. Ardizzone, Emerging pollutant mixture mineralization by TiO$_2$ photocatalysts. The role of the water medium, *Photochem. Photobiol. Sci.*, 2017, **16**, 60–66.

37 W. Cao, T. Huang, X. H. N. Xu and H. E. Elsayed-Ali, Localized surface plasmon resonance of single silver nanoparticles studied by dark-field optical microscopy and spectroscopy, *J. Appl. Phys.*, 2011, **109**, 034310.

38 N. Attarchi, M. Montazer and T. Toliyat, Ag/TiO$_2$/β-CD nano composite: preparation and photo catalytic properties for methylene blue degradation, *Appl. Catal., A*, 2013, **467**, 107–116.

39 H. N. Tien, V. H. Luan, L. T. Hoa, N. T. Khoa, S. H. Hahn, J. S. Chung, E. W. Shin and S. H. Hur, One-pot synthesis of a reduced graphene oxide-zinc oxide sphere composite and its use as a visible light photocatalyst, *Chem. Eng. J.*, 2013, **229**, 126–133.

40 J. T. Abdalla, J. Wang and D. Wang, Effect of Ag/rGO on the Optical Properties of Plasmon-Modified SnO$_2$ Composite and Its Application in Self-Powered UV Photodetector, *Crystals*, 2019, **9**, 648.

41 S. Nayak, L. Mohapatra and K. Parida, Visible light-driven novel g-C$_3$N$_4$/NiFe-LDH composite photocatalyst with enhanced photocatalytic activity towards water oxidation and reduction reaction, *J. Mater. Chem. A Mater.*, 2015, **3**, 18622–18635.

42 N. A. M. Barakat and H. Y. Kim, Effect of silver-doping on the crystal structure, morphology and photocatalytic activity of TiO$_2$ nanofibers, *IOP Conf. Ser. Mater. Sci. Eng.*, 2012, **40**, 012003.

43 H. Tian, C. Wan, X. Xue, X. Hu and X. Wang, Effective electron transfer pathway of the ternary TiO$_2$/RGO/Ag nanocomposite with enhanced photocatalytic activity under visible light, *Catalysts*, 2017, **7**, 156.

44 W. Sun, Q. Meng, L. Jing, L. He and X. Fu, Synthesis of long-lived photogenerated charge carriers of Si-modified α-Fe$_2$O$_3$ and its enhanced visible photocatalytic activity, *Mater. Res. Bull.*, 2014, **49**, 331–337.

45 G. T. S. How, A. Pandikumar, H. N. Ming and L. H. Ngee, Highly exposed {001} facets of titanium dioxide modified with reduced graphene oxide for dopamine sensing, *Sci. Rep.*, 2014, **4**, 2–9.

46 S. Dai, Y. Wu, T. Sakai, Z. Du, H. Sakai and M. Abe, Preparation of highly crystalline TiO$_2$ nanostructures by acid-assisted hydrothermal treatment of hexagonal-structured nanocrystalline titania/cetyltrimethyammonium bromide nanoskeleton, *Nanoscale Res. Lett.*, 2010, **5**, 1829–1835.

47 R. Geng, J. Yin, J. Zhou, T. Jiao, Y. Feng, L. Zhang, Y. Chen, Z. Bai and Q. Peng, In situ construction of Ag/TiO$_2$/g-C$_3$N$_4$ heterojunction nanocomposite based on hierarchical co-assembly with sustainable hydrogen evolution, *Nanomaterials*, 2020, **10**, 1.

48 S. Athithya, V. S. Manikandan, S. K. Harish, K. Silambarasan, S. Gopalakrishnan, H. Ikeda, M. Navaneethan and J. Archana, Plasmon effect of Ag nanoparticles on TiO$_2$/rGO nanostructures for enhanced energy harvesting and environmental remediation, *Nanomaterials*, 2023, **13**, 1–16.

49 A. Bokare, S. Chinnusamy and F. Erogbogbo, TiO$_2$-graphene quantum dots nanocomposites for photocatalysis in energy and biomedical applications, *Catalysts*, 2021, **11**, 1–51.

50 Y. Zhang, Q. Li, Q. Gao, S. Wan, P. Yao and X. Zhu, Preparation of Ag/β-cyclodextrin co-doped TiO$_2$ floating photocatalytic membrane for dynamic adsorption and photoactivity under visible light, *Appl. Catal., B*, 2020, **267**, 118715.

51 X. Zhan, C. Yan, Y. Zhang, G. Rinke, G. Rabsch, M. Klumpp, A. I. Schäfer and R. Dittmeyer, Investigation of the reaction kinetics of photocatalytic pollutant degradation under defined conditions with inkjet-printed TiO$_2$ films – from batch to a novel continuous-flow microreactor, *React. Chem. Eng.*, 2020, **5**, 1658–1670.

52 D. Chatterjee and A. Mahata, Demineralization of organic pollutants on the dye modified TiO$_2$ semiconductor particulate system using visible light, *Appl. Catal., B*, 2001, **33**, 119–125.

53 I. Prabha and S. Lathasree, Effective photocatalytic demineralization of reactive red 198 utilizing nanocomposite particles under UV light irradiation, *J. Ind. Chem. Soc.*, 2017, **94**, 269–277.

54 V. Lalan, V. P. Mahadevan Pillai and K. G. Gopchandran, Enhanced electron transfer due to rGO makes Ag–CaTiO$_3$@rGO a promising plasmonic photocatalyst, *J. Sci. Adv. Mater. Dev.*, 2022, **7**, 100468.

55 V. Vaiano, O. Sacco, G. Di Capua, N. Femia and D. Sannino, Use of visible light modulation techniques in urea photocatalytic degradation, *Water*, 2019, **11**, 1642.

56 X. Xu, Y. Sun, Z. Fan, D. Zhao, S. Xiong, B. Zhang, S. Zhou and G. Liu, Mechanisms for ˙O$_2$$^-$ and ˙OH production on flowerlike BiVO$_4$ photocatalysis based on electron spin resonance, *Front. Chem.*, 2018, **6**, 1–12.